We are IntechOpen, the world's leading publisher of Open Access books Built by scientists, for scientists

4,800
Open access books available

122,000
International authors and editors

135M
Downloads

Our authors are among the

154
Countries delivered to

TOP 1%
most cited scientists

12.2%
Contributors from top 500 universities

WEB OF SCIENCE™

Selection of our books indexed in the Book Citation Index in Web of Science™ Core Collection (BKCI)

Interested in publishing with us?
Contact book.department@intechopen.com

Numbers displayed above are based on latest data collected.
For more information visit www.intechopen.com

6

Numerical Simulations of Nano-Scale Magnetization Dynamics

Paul Horley[1], Vítor Vieira[2], Jesús González-Hernández[1], Vitalii Dugaev[2,3] and Jozef Barnas[4]
[1]*Centro de Investigación en Materiales Avanzados, Chihuahua / Monterrey*
[2]*CFIF, Instituto Superior Técnico, Universidade Técnica de Lisboa, Lisboa*
[3]*Department of Physics, Rzeszów University of Technology, Rzeszów*
[4]*Department of Physics, Adam Mickiewicz University*
[1]*México*
[2]*Portugal*
[3,4]*Poland*

1. Introduction

The discovery of the giant magnetoresistance (Baibich et al., 1988) attracted much scientific interest to the magnetization dynamics at the nano-scale, which eventually led to the formation of a new field – spintronics – aiming to join the conventional charge transfer electronics with spin-related phenomena. The characteristics of spintronic devices (Žutic, Fabian & Das, 2004) are very attractive, including extremely small size (nanometer scale), fast response time and high operating frequencies (on the GHz domain), high sensitivity and vast spectrum of possible applications ranging from magnetic memories (based on magnetization reversal) to microwave generators (involving steady magnetization precession) (Kiselev et al., 2003). The design of these devices, together with the resolution of many problems required for full harvest of spin transport effects in traditional silicon-based semiconductor electronics, is greatly aided by theoretical studies and numerical simulations. For these, one should use adequate models describing magnetization dynamics at the desired scale. If we go down to atomic level, the modelling from first-principles is obligatory. Despite a huge progress in this field (and significant improvement of the computational power of modern equipment), these calculations are far from being real-time and can embrace only a limited amount of particles. Increasing the size of the computational cell to several nanometers, it is possible to introduce the micromagnetic modelling technique, for which every ferromagnetic particle is characterized by an average magnetic moment **M**. These moments can interact with each other by short and long range forces due to exchange coupling and dipole-dipole interactions. The evolution of the individual particle is governed by the Landau-Lifshitz-Gilbert (LLG) equation – a semi-classical approximation allowing to represent the time evolution of the magnetization vector **M** depending on applied magnetic fields and spin-polarized currents passing through the particle.
Micromagnetics is a rapidly-developing field allowing tackling many serious problems (Fidler & Schrefl, 2000; Berkov & Gorn, 2006). It is far simpler to implement in comparison

with first principles calculations, so that modern computers can be efficiently used even for 3D micromagnetic simulations of large systems (Scholz et al., 2003; Vukadinovic & Boust, 2007). The amount of calculations required strongly depends on the space discretization of the modelled object. For maximum accuracy, the volume of the magnetic body is divided into a set of triangular prisms according to different tessellation algorithms. The system thus becomes represented by a set of magnetization vectors $\mathbf{M}_i$ corresponding to the nodes of the resulting mesh. The evolution of the system can be obtained by solving the LLG equation using finite element methods (Koehler & Fredkin, 1992; Szambolics et al., 2008), which may involve re-structurization of the mesh to account for variation of the magnetization distribution inside the sample. These calculations require considerable computational resources and thus are usually performed on multi-processor computers or clusters thereof.

The calculations can be optimized for the case of regular meshes, with the simplest numerical procedures available for cubic (3D) and square (2D) grids. In this case, the cumbersome finite element methods can be substituted by simpler finite difference methods, which benefit from pre-calculated coefficients for the derivatives required in the calculation of near and far range interactions between the magnetic particles. The most time consuming part of micromagnetic simulations concerns long-range interactions contributing to the demagnetizing field. As this is formed by every particle belonging to the object, one should calculate a complete convolution for every magnetic moment $\mathbf{M}_i$. In the case of uniform grids, these calculations can be much simplified recalling that convolution in normal space correspond to multiplication in the Fourier space. Thus, one has to Fast Fourier Transform (FFT) the components of the demagnetizing field (Schabes & Aharoni, 1987) and $\mathbf{M}_i$ for every grid point, multiply them and inverse-FFT the result to obtain the demagnetizing field. The other option is to use the fast multipole algorithm (Tan, Baras & Krishnaprasad, 2000), which can be also accelerated with the Fast Fourier Transform (Liu, Long, Ong & Li, 2006). The downside of uniform square grids is the complication to represent non-rectangular objects. Even at small grid step the curves or lines that are not perpendicular to the grid directions generate the staircase structure, which is artificial and has no counterpart in the modelled ferromagnetic objects. This staircase acts as a nucleation source of magnetization vortices, which may lead to incorrect simulation data suggesting vortex-assisted magnetization dynamics (García-Cervera, Gimbutas & Weinan, 2003) while the real systems may display coherent magnetization rotation. To solve this issue (and to retain the benefits of fast calculation of demagnetizing fields using FFT) one can introduce corrections for the boundary cells (Parker, Cerjan & Hewett, 2000; Donahue & McMichael, 2007), allowing to take into account the real shapes in place of its cubic or square cells.

However, the general methodology of solving the LLG equation can be discussed for simpler models without the need to consider convolution, tessellation or grid discretization errors for smooth contours. Actually, we can consider a single magnetic moment obeying the LLG equation, which is the situation that can be found on a larger scale – thin magnetic films with dimensions of dozens of nanometers. Stacking several ferromagnetic films together and separating them by a non-magnetic spacer, one can obtain the simplest spintronic device, a spin valve. The layers composing the valve serve different purposes and because of this should have different thickness. The thicker layer is bulk enough to preclude re-orientation of its magnetization vector by an applied magnetic field. To improve its stability, it is usually linked with an anti-ferromagnetic interaction with yet another substrate layer. The role of this fixed layer consists in aligning the magnetic moments of the passing carriers, so that the current injected into the second, much thinner analyzer layer,

will be spin-polarized. The analyzer layer, on the contrary, can be easily influenced by the applied magnetic field, and it will manage to change its magnetization as a whole – thus representing a *macrospin* (Xiao, Zangwill & Stiles, 2005). The experimental studies of spin valves successfully confirmed the theoretical predictions made in the macrospin approximation, including precessional and ballistic magnetization reversal, two types of steady magnetization oscillations – in-plane and out-of-plane, as well as magnetization relaxation to an intermediate canted state.

The detailed discussion of the magnetization dynamics is out of the scope of this chapter; however, it is imperative to consider various representations of the main differential equations governing the motion of the magnetization vector, as well as to discuss the numerical methods for their appropriate solution. In particular, the modelling of the temperature influence over the system, which is usually done adding a thermal noise term to the effective field, leading to stochastic differential equations that require special numerical methods to solve them.

2. Landau-Lifshitz-Gilbert equation

Let us consider a magnetic particle characterized by a magnetization vector **M**, and subjected to the action of an effective magnetic field **H** and spin-polarized current **J**, rendering magnetic torques on the system. The changes of magnetization with time are governed by the Landau-Lifshitz-Gilbert equation:

$$\frac{d\mathbf{M}}{dt} = -\gamma \mathbf{M} \times \mathbf{H} + \frac{\gamma}{M_S} \mathbf{M} \times (\mathbf{M} \times \mathbf{J}) + \frac{\alpha}{M_S} \mathbf{M} \times \frac{d\mathbf{M}}{dt} \tag{1}$$

The first term in the right side of the equation corresponds to the Larmor precession around the magnetic field direction, featuring a gyromagnetic ratio $\gamma = 2.21 \times 10^5$ m/(As). The second term, proposed by Slonczewski (1996), describes the spin torque rendered by the injected current **J**. The third term was introduced by Gilbert (2004); it presents a phenomenological description of magnetization damping, caused by dissipation of the macrospin energy due to lattice vibrations, formation of spin waves and so on (Saradzhev et al., 2007). Thus, in the absence of energy influx (provided by injected current), the system should relax to a stable state. As the magnetic motion is effectively controlled by the interplay of driving and damping forces, it is natural to suggest a model of viscous damping with a coefficient α multiplied by the rate of change of the magnetization. On the other hand, it is unclear if a constant damping coefficient is sufficient to reproduce accurately the magnetization dynamics (Mills & Arias, 2006), which may require additional tweaking such as making α dependent on the orientation of the magnetization vector (Tiberkevich & Slavin, 2007).

An essential feature of the LLG equation is that unconditionally preserves the length of the magnetization vector, which corresponds to the saturation magnetization M_S of the material. All possible magnetization dynamics is thus confined to the re-orientation of **M**, which can be visualized as a phase trajectory formed by the motion of the tip of the magnetization vector over the sphere with radius M_S. The effective magnetic field

$$\mathbf{H} = \mathbf{H}_{EXT} - (C_{DEM} M_X \mathbf{e}_X - C_{ANI} M_Z \mathbf{e}_Z) / M_S \tag{2}$$

is composed of applied external field $\mathbf{H}_{EXT}$, demagnetization field with a constant C_{DEM} (valid for thin film approximation), and anisotropy field with coefficient $C_{ANI} = 2K_1/\mu_0 M_S$

with easy axis anisotropy constant K_1. For the case of very thin ferromagnetic films the easy magnetization axis will be located in the film plane, while the demagnetizing field will penalize deviations of the magnetization from this plane. Therefore, in our case the ferromagnetic film is set in the plane YZ, with an easy magnetization axis directed along the axis Z. The injected spin-polarized current is scaled with $\hbar\eta / 4eVK_1$, with spin polarization degree η and volume of the analyzer layer V.

Taking a cross product of the LLG equation with $d\mathbf{M}/dt$, re-arranging the terms, and introducing the torque-inducing vectors $\mathbf{\Lambda} = \mathbf{H} + \alpha\mathbf{J}$ and $\mathbf{\Delta} = \mathbf{J} - \alpha\mathbf{H}$, one can transform the equation into the Landau explicit form, with the time derivative $d\mathbf{M}/dt$ on the r.h.s. only:

$$\frac{1}{\gamma_1}\frac{d\mathbf{M}}{dt} = -\mathbf{M}\times\mathbf{\Lambda} + \frac{1}{M_S}\mathbf{M}\times(\mathbf{M}\times\mathbf{\Delta}) \tag{3}$$

with a re-normalized gyromagnetic ratio $\gamma_1 = \gamma / (1+\alpha^2)$. For the calculations illustrated in this paper, we have used the common parameters for Co/Cu/Co spin valves (Kiselev et al., 2003): analyzer layer with dimensions 91×50×6 nm^3, C_{ANI} = 500Oe, $4\pi M_S$ = 10kOe, and α = 0.014. The main dynamic modes that can be obtained from the LLG equation include magnetization reversal between the stationary states $M_Z = \pm M_S$, relaxation of the magnetization to intermediate canted states, and steady magnetization precession. To illustrate the ranges of variables H and J for which these states take place, it is useful to construct a dynamic diagram of the system (Fig. 1). The task can be simplified by choosing the proper numerical characteristics allowing clear distinction between the corresponding states. The situation with up/down and canted orientation of **M** is easily resolved by monitoring the average value of the magnetization component along the easy axis, $\langle M_Z \rangle$. In this way one can easily discover low-field and high-field magnetization switching. The former occurs when the applied field overcomes the anisotropy constant C_{ANI}, which is marked with a thick horizontal line in Fig. 1. Below it, the magnetization vector remains in the initial state pointing down. Above this line, the magnetization points upwards (Fig. 1a). Under high fields and applied currents, it is also possible to obtain magnetization pointing down (Fig. 1g). The transition between these two states comes through slow magnetization reversal with phase trajectories practically covering the entire sphere (Fig. 1h). Lowering the field, one can shift the stable point from the stationary states $M_Z = \pm M_S$, reaching a canted state (Fig. 1e-g). The variation of current "opens" the canted state into a periodic trajectory (Fig. 1d). At this point, the observation of $\langle M_Z \rangle$ does not suffice to distinguish between oscillating and non-oscillating states, because the average for a cyclic orbit gives a position of its centre, as if the system converges to the canted state. The situation becomes more complicated for complex phase portraits that contain several loops (Fig. 1b). To solve this problem, it is useful to calculate the Hausdorff dimension (Lichtenberg & Lieberman, 1983):

$$D_H = -\lim_{\varepsilon\to 0}\frac{\log N}{\log \varepsilon} \tag{4}$$

where N is the number of cubes with side ε required to cover the phase portrait. If we are considering the stationary state, when the magnetization vector is fixed, the corresponding phase portrait will be a point with $D_H = 0$. When the system performs magnetization oscillations along a fixed trajectory, the Hausdorff dimension will be equal

or above unity. The higher values of D_H will be achieved for higher number of loops, and when these will eventually cover the whole sphere, the dimension should reach the value of 2.

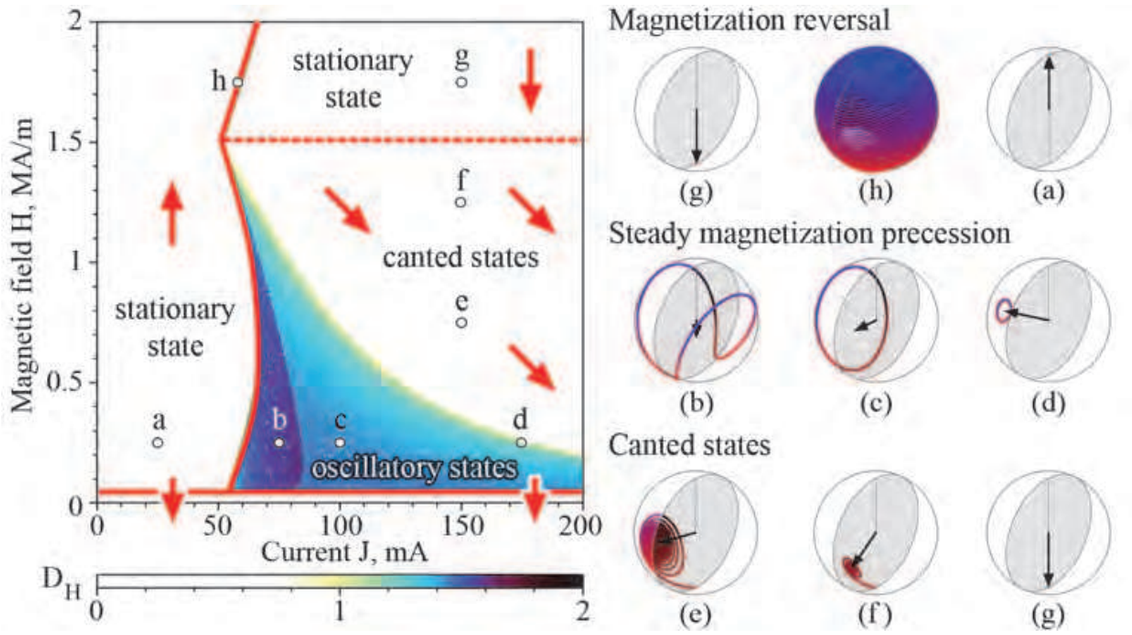

Fig. 1. Dynamic diagram of macrospin system for different applied magnetic field and injected spin-polarized current. The right panel shows the characteristic phase portraits with grey oval corresponding to film plane *YZ*, and an arrow denoting averaged magnetization.

The macrospin model features two types of steady oscillations. In the simplest case, the magnetization vector precesses around the canted axis, considerably deviating from the film plane (Fig. 1c, d), hence the name – out-of-plane precession (OPP). For lower values of injected current, the precession cycle splits into a butterfly-shaped curve (Fig. 1b), symmetric regarding the film plane. Thus, despite magnetization vector deviates from the film plane for certain periods, the average over the whole oscillation cycle will remain parallel to the axis *Z*, so that this type of phase portrait is called in-plane precession (IPP). The dynamic diagram shows how efficient is the use of the Hausdorff dimension for visual separation of the parameter areas where in-plane and out-of-plane precession takes place; it also works fine for complicated cases of multi-loop phase portraits triggered by pulsed fields and currents (see Horley et al., 2008). Now, having the idea of what to expect from the solution of the LLG equation, let us discuss in detail its different representations (including strengths and weaknesses thereof from the computational point of view), as well as numerical methods required for the most efficient and accurate solution of this equation.

2.1 Cartesian projection

As we are studying the evolution of the magnetization in three-dimensional space, it is straightforward to re-write the LLG for the Cartesian system as a set of ordinary differential equations regarding the individual components of the magnetization vector M_X, M_Y and M_Z:

$$\begin{aligned}\frac{dM_X}{dt} &= -\gamma_1(M_Y\Lambda_Z - M_Z\Lambda_Y - M_X\Xi + M_S\Delta_X)\\ \frac{dM_Y}{dt} &= -\gamma_1(M_Z\Lambda_X - M_X\Lambda_Z - M_Y\Xi + M_S\Delta_Y)\\ \frac{dM_Z}{dt} &= -\gamma_1(M_X\Lambda_Y - M_Y\Lambda_X - M_z\Xi + M_S\Delta_Z)\end{aligned} \tag{5}$$

with $\Xi = (\mathbf{M}\cdot\Delta)/M_S$. The Cartesian representation of the LLG is very easy to implement; since it uses only basic arithmetic operations, ensuring very fast calculations. However, the length of the magnetization vector is not unconditionally preserved in the straightforwardly discretized version of these equations, so that even with a small integration step the system will diverge after a few dozens of iterations. The common methodology to keep the length of **M** constant consists in re-normalization of the magnetization after some (or each) iteration. However, such an approach is often criticized: when the magnetization vector goes out of the sphere with radius M_S, it becomes difficult to say if it is adequate to solve the situation only by re-scaling of the vector without resorting to re-orientation of **M**.

In fact, the condition $\mathbf{M}^2 = M^2$ imposes a series of conditions starting with $\mathbf{M}\cdot\frac{d\mathbf{M}}{dt} = 0$ and $\mathbf{M}\cdot\frac{d^2\mathbf{M}}{dt^2} = -\left(\frac{d\mathbf{M}}{dt}\right)^2$. In the renormalization procedure one has

$$\mathbf{M}(t+\Delta t) \approx \frac{\mathbf{M}(t) + \frac{d\mathbf{M}}{dt}\Delta t}{\sqrt{1 + \frac{1}{M^2}(\frac{d\mathbf{M}}{dt})^2(\Delta t)^2}} \approx \mathbf{M}(t) + \frac{d\mathbf{M}}{dt}\Delta t - \frac{1}{2}\frac{1}{M^2}(\frac{d\mathbf{M}}{dt})^2\mathbf{M}(t)(\Delta t)^2 \tag{6}$$

so that the requirement of second order restriction is automatically implemented, fixing the component $\frac{1}{2}\frac{d^2\mathbf{M}}{dt^2}\Delta t^2$ along the direction of $\mathbf{M}(t)$ itself; however, it is not fixed completely, as we will see in section 2.4. Thus, one will need reasonably small time steps (below pico-second level) to replicate the experimental system behaviour with an acceptable precision.

2.2 Spherical projection

The constant length of the magnetization vector invites to use spherical coordinates, describing the orientation of the magnetization vector with zenith and azimuth angles θ and φ. The LLG equation in this projection has the following form:

$$\begin{aligned}\frac{d\theta}{dt} &= \gamma_1[-\Lambda_X\sin\varphi + \Lambda_Y\cos\varphi - \cos\theta(\Delta_X\cos\varphi + \Delta_Y\sin\varphi) + \Delta_Z\sin\theta]\\ \sin\theta\frac{d\varphi}{dt} &= -\gamma_1[\cos\theta(\Lambda_X\cos\varphi + \Lambda_Y\sin\varphi) - \Lambda_Z\sin\theta - \Delta_X\sin\varphi + \Delta_Y\cos\varphi]\end{aligned} \tag{7}$$

Despite the system is comprised only of two equations, it includes numerous trigonometric functions. As one immediately sees, the quantities $\sin\theta$, $\sin\varphi$, $\cos\theta$ and $\cos\varphi$ enters several times into the equations, calling for obvious optimization by calculating these quantities only once per iteration. However, as we need to take into account magnetic anisotropy as

well as demagnetizing field, the equations corresponding to (1) in the spherical coordinates representation would be loaded with trigonometric functions, which require a considerable calculation time. Additionally, one may want to obtain the projections of the magnetization vector (e.g., for visualization of the phase portrait):

$$\begin{aligned} M_X &= M_S \sin\theta\cos\varphi \\ M_Y &= M_S \sin\theta\sin\varphi \\ M_Z &= M_S \cos\theta \end{aligned} \tag{8}$$

Such pronounced use of trigonometric functions slows down the calculation process considerably. In comparison with the Cartesian coordinate representation (including re-normalization of magnetization vector on every step), the numerical solution of the LLG in the spherical representation is about six times slower (Horley et al., 2009).

2.3 Stereographic projection

Aiming to optimize the calculation time, one seeks to keep the LLG equation reduced to the lower number of components and avoiding, if possible, the use of special functions. One solution to this problem is the use of the stereographic projection mapping the sphere into a plane with the complex variable $\zeta = \tan(\frac{1}{2}\theta)e^{i\varphi}$. The LLG equation has the following form in the stereographic projection (Horley et al., 2009):

$$\frac{2}{1+\zeta^*\zeta} = \gamma_1[-(J_{S+} + i\varsigma H_{S+}) + \alpha(H_{S+} - i\varsigma J_{S+})] \tag{9}$$

The quantities marked with subscript "S_+" correspond to spherical components of the vector **H** (and similarly **J**) in a rotated basis, defined by a rotation transforming $\mathbf{e}_Z$ into $\mathbf{e}_r$, so that $H_{S+} = (H_+ - \zeta^2 H_- - 2\varsigma\alpha H_0)/(1+\zeta^*\zeta)$. The variables H_+, H_- and H_0 represent the irreducible spherical components of a Cartesian tensor (Normand & Raynal, 1982). If the magnetization trajectory is limited only to the upper or to the lower hemisphere, the task of choosing the proper projector pole is trivial. However, if we want to study the magnetization reversal with the phase point passing from one pole to another, the corresponding equation written for a single projection pole will cause numerical overflow. The situation can be solved by dynamical switching of the projector pole. The variable $\varsigma = \pm 1$ denotes the projector pole (lower or upper). It is important to mention that for $\varsigma = 1$ the upper pole will correspond to $\zeta = 0$, while the lower (projector) pole will cause $\zeta \to \infty$. Switching the projector pole to upper one ($\varsigma = -1$), one should recalculate the projection variable as $\zeta' = 1/\zeta^*$, after which the value $\zeta = 0$ will correspond to the lower, and $\zeta \to \infty$ to the upper pole. Thus, for phase portraits situated in the upper and lower hemisphere one will have two projections that merge at the equatorial line. It is convenient to present both projections in different colours (depending on the projection pole used) in the same plot, as it is illustrated in Figure 2 for the case of IPP and OPP cycles. This approach simplifies the visualization of the phase portraits, offering a useful "recipe" for obtaining a clear 2D plot of a 3D magnetization curve. The superimposed plots may become complicated for phase portraits composed of numerous loops, but this situation does not occur in a system subjected to constant fields and currents (Horley et al., 2008).

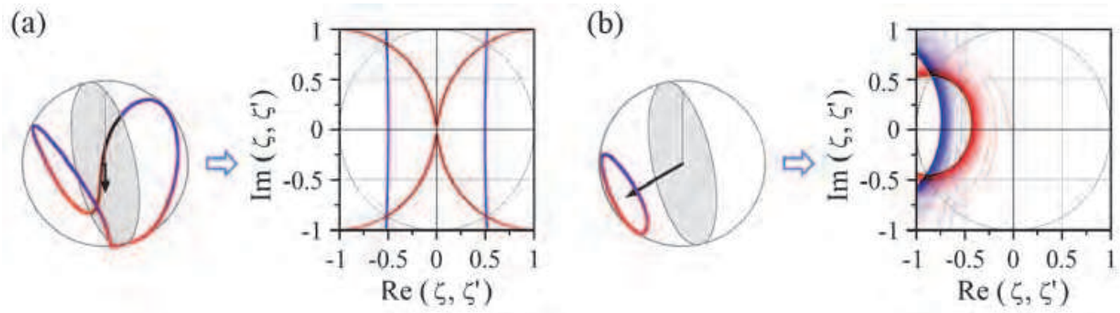

Fig. 2. Stereographic projection of in-plane (a) and out-of-plane (b) steady precession of a macrospin. Red curves show the projection from the upper pole, blue curves correspond to projection from the lower pole. The dotted grey circle represents the equator of the sphere $|\mathbf{M}| = const$, normalized over saturation magnetization M_S.

To improve the calculation performance for the LLG equation written in the stereographic projection, it is important to optimize the procedure for projector pole switching. Our previous studies have shown that it is not productive to switch the pole each time the magnetization trajectory crosses the equator (Horley et al., 2009). A more useful approach consists in the introduction of a certain threshold value $|\zeta|_S$, after crossing which the pole switching should be performed. Our numerical tests shown that threshold values of $|\zeta|_S = 1000$ (corresponding to the zenith angle $\theta = 0.99936\pi$) boosts the calculation performance, allowing to achieve five-time speed-up of the simulation comparing with the spherical representation of the LLG equation. Increase of $|\zeta|_S$ by five orders of magnitude does not lead to any further improvement of calculation speed.

2.4 Frenet-Serret projection

Another representation of a curve in three-dimensional space can be made in the Frenet-Serret reference frame consisting of tangent vector **T**, normal **N** and binormal $\mathbf{B} = \mathbf{T} \times \mathbf{N}$. The equations governing the variation of these vectors for a curve parameterized by the arc length s are the following

$$\frac{d\mathbf{T}}{ds} = \chi \mathbf{N}, \qquad \frac{d\mathbf{N}}{ds} = -\chi \mathbf{T} + \tau \mathbf{B}, \quad \frac{d\mathbf{B}}{ds} = -\tau \mathbf{N} \tag{10}$$

where χ and τ are the curvature and torsion of the curve, given by

$$\chi = \frac{\left| \frac{d\mathbf{M}}{dt} \times \frac{d^2\mathbf{M}}{dt^2} \right|}{\left| \frac{d\mathbf{M}}{dt} \right|^3}, \qquad \tau = \frac{\left(\frac{d\mathbf{M}}{dt} \times \frac{d^2\mathbf{M}}{dt^2} \right) \cdot \frac{d^3\mathbf{M}}{dt^3}}{\left| \frac{d\mathbf{M}}{dt} \times \frac{d^2\mathbf{M}}{dt^2} \right|^2} \tag{11}$$

They depend on higher order derivatives (second or second and third), putting more demanding requirements on the precision of the numerical integration method used. It is interesting to use these two scalars (χ and τ) for characterization of the LLG solutions. Using the above equations one can write the lowest terms in the time development of the magnetization vector as

$$\mathbf{M}(t+\Delta t)=\mathbf{M}(t)+\frac{ds}{dt}\mathbf{T}\Delta t+\frac{1}{2}\left(\frac{d^2s}{dt^2}\mathbf{T}+\chi\left(\frac{ds}{dt}\right)^2\mathbf{N}\right)(\Delta t)^2+\cdots \tag{12}$$

The tangent component of the second order correction vanishes if one uses the arc length instead of time in the curve parameterization. Since the vectors **T**, **N** and **B** form a complete basis, the vector **M** is, at each time, a linear combination of the vectors **N** and **B**. Using the Frenet-Serret equations one finds that

$$\mathbf{M}=-\frac{1}{\chi}\mathbf{N}+\frac{\chi'}{\chi^2\tau}\mathbf{B} \tag{13}$$

where the prime denotes differentiation with respect to the arc length, together with the condition $\left(\frac{\chi'}{\chi^2\tau}\right)'=\frac{\tau}{\chi}$, which also follows from the constraint $\mathbf{M}^2 = const$. One sees that the second order condition $\mathbf{M}\cdot\frac{d^2\mathbf{M}}{dt^2}=-\left(\frac{d\mathbf{M}}{dt}\right)^2$ is automatically satisfied since the parallel components of **M** and $\frac{d^2\mathbf{M}}{dt^2}$ in the Frenet-Serret reference frame (i.e. along **N)** are inversely proportional. Alternatively, one can say that the renormalization of the magnetization vector fixes the component of $\frac{d^2\mathbf{M}}{dt^2}$ along **M**, but that it misses to fix the component along the direction orthogonal to **M** and **T**.

The analytical expressions of the curvature and torsion in the absence of applied current are

$$\chi=\frac{\sqrt{\gamma_1^2+\lambda^2+\zeta^2}}{\sqrt{\gamma_1^2+\lambda^2}} \tag{14}$$

$$\tau=\frac{\sqrt{\gamma_1^2+\lambda^2}}{\gamma_1^2+\lambda^2+\zeta^2}\frac{d\zeta}{ds} \tag{15}$$

Equations (14) and (15) use re-normalized gyromagnetic ratio $\gamma_1 = \gamma/(1+\alpha^2)$, $\lambda=\alpha\gamma_1$ and the variable ζ given by the formula

$$\zeta=\frac{1}{|\mathbf{m}\times\mathbf{H}|}\left[\gamma_1(\mathbf{m}\cdot\mathbf{H})+\sqrt{\gamma_1^2+\lambda^2}\left(\mathbf{m}_1\cdot\frac{d\mathbf{H}}{ds}\right)\right]. \tag{16}$$

Its derivative along the trajectory can be found as

$$\begin{aligned}\frac{d\zeta}{ds}=\frac{\sqrt{\gamma_1^2+\lambda^2}}{|\mathbf{m}\times\mathbf{H}|}\Bigg[&\frac{\lambda}{\gamma_1^2+\lambda^2}(\zeta\,\mathbf{m}-\gamma_1\mathbf{m}_2)\cdot\mathbf{H}\\&+\frac{2}{\sqrt{\gamma_1^2+\lambda^2}}(\gamma_1\,\mathbf{m}+\zeta\,\mathbf{m}_2)\cdot\frac{d\mathbf{H}}{ds}+\left(\mathbf{m}_1\cdot\frac{d^2\mathbf{H}}{ds^2}\right)\Bigg]\end{aligned} \tag{17}$$

The quantities $\mathbf{m}$, $\mathbf{m}_1$ and $\mathbf{m}_2$ entering equations (16) and (17) are defined as

$$\mathbf{m} = \frac{\mathbf{M}}{M_S}, \quad \mathbf{m}_1 = \frac{\mathbf{m}\times\mathbf{H}}{|\mathbf{m}\times\mathbf{H}|}, \quad \mathbf{m}_2 = \mathbf{m}\times\frac{\mathbf{m}\times\mathbf{H}}{|\mathbf{m}\times\mathbf{H}|} \tag{18}$$

It is worth noting that formulas (14) and (15) are derived for the case when macrospin is subjected only to an external magnetic field. This model can be easily extended to include the Slonczewski torque term into the LLG equation by noticing that the spin-polarized current torque in (1) can be formally incorporated into the precession term, which will result in replacement of the applied field $\mathbf{H}$ by the effective field $\mathbf{H}_{EFF}$:

$$\mathbf{H}_{EFF} = \mathbf{H} - \frac{\mathbf{M}}{M_S}\times\mathbf{J} \tag{19}$$

In a similar manner, the equation (3) can be rewritten for the case of the injected spin-polarized current with the same effective field replacement according to formula (19). This methodology can be used to incorporate the Slonczewski torque into the formulas (14) and (15) for torsion and curvature. Due to simplicity of this replacement, it was deemed unnecessary to present the modified versions of formulas (14) and (15) here.

The Frenet-Serret frame allows analysis of the magnetization curve properties, shown in Figs. 3 and 4 for in-plane and out-of-plane precession cases, respectively. To be able to carry out the comparison, it was necessary to adequate the phase portraits that are characterized by different precession frequencies. To do this, we separated a single precession cycle using the following algorithm:

1. for each magnetization component m_i, find the local minimum at time a_i;
2. find the second local minimum at time b_i;
3. find the estimated period as $c_i = b_i - a_i$;
4. choose the variable with the largest c_i and consider the portion of a phase portrait formed by the data limited by time moments a_i and b_i.

To visualize the values of velocity, curvature and torsion (VCT) directly on the phase portrait, we faced the following difficulty. It is possible to code these quantities as colours, but it may be quite complicated to interpret them as, for example, the torsion can be positive or negative. Thus, it would be preferable to show the corresponding quantities as vectors. As they give the local characteristics of the curve, it would be impractical to show them as a tangent vector of varying length. On the contrary, plotting the corresponding quantities along the normal or binormal would be more understandable. It resulted that namely plotting VCT along the normal offered a more straightforward intuitive interpretation. Thus, if the local torsion is positive, it would be plotted as a vector pointing inside the curve; if the torsion is negative, the corresponding vector will point outside of the curve. To visualize the smooth variation of VCT along the phase portrait, it proved considerably useful to plot an enveloping curve for every calculated phase point, introducing only several reference vectors denoting the behaviour of the local velocity, curvature and torsion.

The resulting plots allow clear analysis and interpretation of the VCT parameters. The largest rate of magnetization variation (velocity of the phase point) is observed at the upper part of the "wings" of the butterfly-shaped phase portrait (Fig. 3a, point A). This is understandable as the stationary solutions of the LLG include upper and lower poles of the

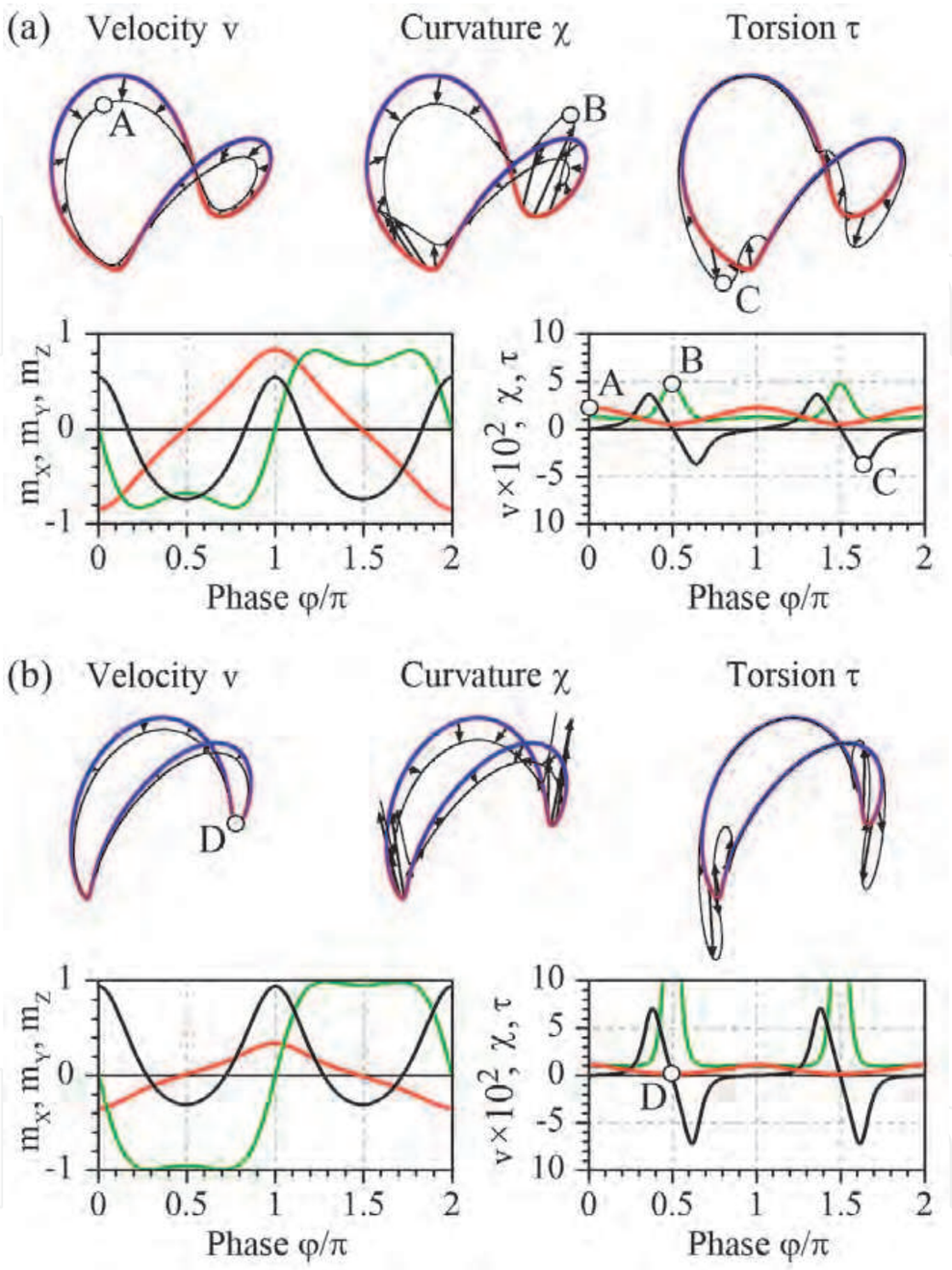

Fig. 3. Velocity, curvature and torsion of in-plane precession phase portrait calculated for a) H = 0.4 MA/m, J = 69mA; b) H = 0.53 MA/m, J = 64mA. The curve characteristics are plotted as vectors directed along the normal to the curve, not to scale with the phase portrait. The enveloping curve is shown as thin black line. The panels below presents the distribution of normalized magnetization components $m_i = M_i/M_S$ (red – m_X, green – m_Y and black – m_Z) as well as velocity, curvature and torsion (red, green and black, respectively). The characteristic points are marked with letters: A) large velocity; B) large curvature; C) large torsion and D) small velocity and torsion

sphere and canted states, which are located outside of the easy magnetization plane. Thus, passing along the upper part of the trajectory, the phase point travels through the area well away from the stationary points, where the energy gradient is high, causing fast reorientation of the magnetization. Upon approaching to the folding point, the phase point travels closer to the stationary point, resulting in a much slower magnetization variation (Fig. 3b, point D). As the two wings of the phase portrait join at the easy magnetization plane, the curvature of the trajectory will increase significantly (Fig. 3a, point B), becoming higher for smaller separation between the wings (Fig. 3b). At the peak of the curvature and minimum velocity, the torsion changes sign, becoming negative after passing the point with maximum curvature (Fig. 3a, point C). It is worth mentioning that, because the curvature of the phase portrait is always positive, the period of the VCT curves constitutes a half of the total period of in-plane precession oscillations. Thus, one cannot use VCT plots to distinguish between the left and right "wings" of the magnetization curve.

In the case of out-of-plane precession cycle (Fig. 4), the behaviour of the VCT is similar, because the phase point moves in the same energy landscape. When we consider the large precession cycle (Fig. 4a) that corresponds to one of the wings of in-plane precession cycle, one can observe increase of the magnetization precession velocity upon approaching the upper part of the cycle. The lower part, while looking quite smooth, features increase of curvature representing a "relic" of butterfly-shaped phase portrait corresponding to in-plane precession. The small "splash" of torsion is also observable in this part of the phase trajectory. However, if the phase portrait represents a cycle set well away from the easy magnetization plane, the velocity of the phase point will be considerably uniform (Fig. 4b).

The curvature becomes constant and the torsion is vanishing, proving that this phase portrait approaches to a circle lying in a plane, for which, as we know, the curvature is equal to the inverse of the radius and the torsion is zero. Namely this type of oscillations, despite of their modest amplitude, is most promising for microwave generator use, because the time profiles of its magnetization components approach the harmonic signal (Fig. 4b).

3. Numerical methods

A proper choice of the numerical method for the solution of the LLG equation is very important. The straightforward solution to obtain the most accurate results is to apply a higher-order numerical scheme to the equations written in one of the coordinate systems that ensures unconditional preservation of the magnetization vector length. However, depending on the complexity of the system, this approach may require many hours of computer time. The opposite approach consists in the choice of the simplest (first order) numerical method applied to the fastest-to-calculate representation of LLG – the Cartesian coordinates. In this way, the speed of simulations will increase up to an order of magnitude – but alas, the results will be completely flawed even using reasonably small values of the integration step h. Additional problems appear if we want to include the temperature into the model – the resulting LLG equation is stochastic, and correct results can be achieved only using numerical methods converging to the Stratonovich solution. All these details should be taken into account in search of a balance between calculation speed and accuracy.

We will focus here on explicit numerical schemes, which are simpler for implementation as they offer direct calculation of the next point using the current value of the function. Writing the ordinary differential equation as

$$y' = f(t, y(t)) , \tag{20}$$

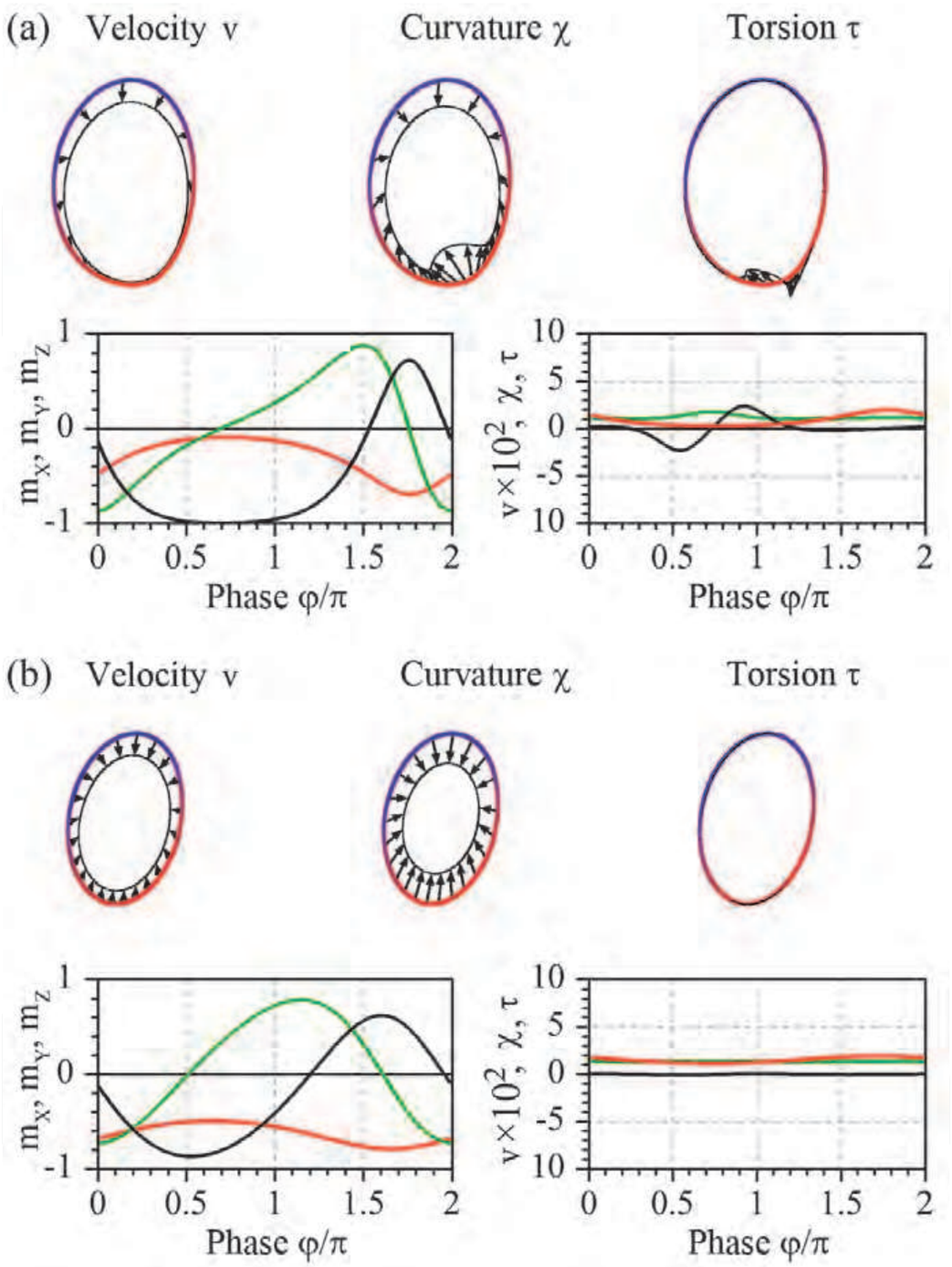

Fig. 4. Velocity, curvature and torsion of out-of-plane phase portrait calculated for a) H = 0.2 MA/m, J = 87mA; b) H = 0.18 MA/m, J = 136mA. Similarly to Fig. 3, the thin black curve envelops the vectors corresponding to aforementioned characteristics of the phase portrait, set along the normal to the curve. The time distribution of normalized magnetization $m_i = M_i/M_S$ (red – m_X, green – m_Y and black – m_Z) and velocity, curvature and torsion (red, green and black, respectively) are given in the bottom panels.

one can obtain the value of the derivative for the point t. Depending on the accuracy required, this value can be used as is or improved introducing intermediate points. Knowing the initial value of the function (Cauchy boundary condition), one can thus obtain the next point and then iterate from there. For simplicity, we will consider here single-step methods that require only information about a single point for the integration of the system.

3.1 First order methods

The simplest integration formula, suggested by Leonhard Euler, straightforwardly uses Eq. (20) to calculate the value of the function in the next point y_{n+1} basing on its current value y_n:

$$y_{n+1} = y_n + hf(t_n, y_n) \tag{21}$$

This approach suffers from the fact that the value of the derivative in the point (y_n, t_n) does not hold for the whole integration step h, resulting in an error $O(h)$. While it can be acceptable for other systems, in the case of the LLG the situation is special due to the fact that the first order methods are insufficient for accurate solution (see discussion after equation (13)). Accumulation of these errors distorts the results, leading to significantly different time evolution of the magnetization. This situation is illustrated in Fig. 5 showing solutions of the LLG calculated with the Euler method and 4th order Runge-Kutta method.

As one can see from the figure, starting from the first peak (t ~ 115ps) the curve obtained with the Euler method deviates; upon reaching the first minimum (t ~ 150ps) the difference with the curve integrated with the Runge-Kutta method already becomes significant. It is necessary to emphasize that the curves shown in Fig. 5 feature different amplitude and frequencies – that is, the solution obtained with the Euler method is much distinct and should be regarded as inadequate. Due to this accuracy issue, the first-order methods should not be used at all for the numerical solution of the LLG equation.

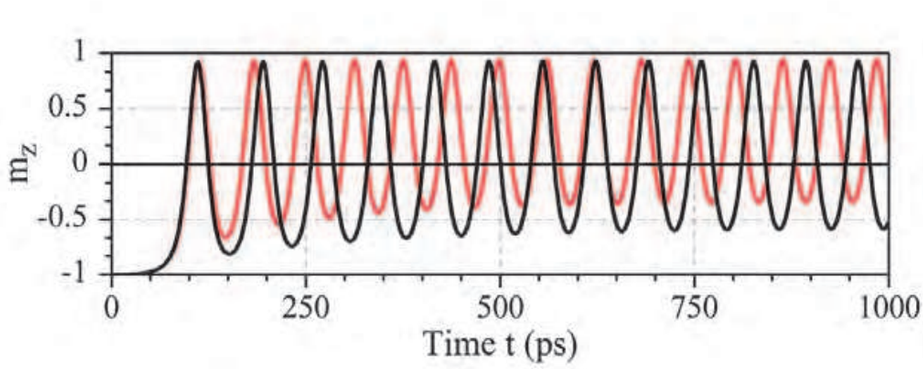

Fig. 5. Comparison of time evolution of normalized magnetization component $m_z = M_Z/M_S$: red curve – integrated with Euler method; black curve – integrated with 4th order Runge-Kutta method. Parameter values: applied magnetic field H = 60kA/m, injected spin-polarized current J = 0.07A, integration step h = 0.5 ps.

3.2 Higher order methods

The simplest way to improve the accuracy of the Euler method is to observe that

$$\begin{aligned} y(t+h) &= y(t) + h\frac{dy}{dt} + \tfrac{1}{2}h^2\frac{d^2y}{dt^2} + O(h^3) \\ &= y(t) + hf(t,y(t)) + \tfrac{1}{2}h^2\left(\frac{\partial f}{\partial t} + \frac{\partial f}{\partial y}f\right) + O(h^3) \\ &= y(t) + h\left[f(t,y(t)) + \tfrac{1}{2}h\left(\frac{\partial f}{\partial t} + \frac{\partial f}{\partial y}f\right)\right] + O(h^3) \\ &= y(t) + hf\left[t + \tfrac{1}{2}h, y(t) + \tfrac{1}{2}hf(t)\right] + O(h^3) \end{aligned} \tag{22}$$

A similar second order integrator is the "modified Euler method" or "Heun method":

$$\widehat{y}_{n+1} = y_n + hf(t_n, y_n), \qquad y_{n+1} = y_n + \tfrac{1}{2}h\left(f(t_n, y_n) + f(t_{n+1}, \widehat{y}_{n+1})\right) \tag{23}$$

which can be interpreted as an predictor-corrector method. It can be obtained formally integrating the differential equation and using then the trapezoidal method to correct the values of the derivative. Higher order integration methods are usually derived choosing a specific form of the integrator with a certain number of points and some free weights which are then chosen to obtain the desired accuracy.

In the framework of the generalization proposed by Carl Runge and Martin Kutta, the Heun method can be classified as a second order Runge-Kutta method. It already has an acceptable accuracy, at the same time featuring considerable calculation speed. The precision of the integrator can be improved by using more intermediate points, leading to the most commonly-used 4th order Runge-Kutta method with total accumulated error $O(h^4)$:

$$\begin{aligned} k_1 &= f(t_n, y_n), \\ k_2 &= f(t_n + \tfrac{1}{2}h, y_n + \tfrac{1}{2}hk_1), \\ k_3 &= f(t_n + \tfrac{1}{2}h, y_n + \tfrac{1}{2}hk_2), \\ k_4 &= f(t_n + h, y_n + hk_3), \\ y_{n+1} &= y_n + \tfrac{1}{6}h(k_1 + 2k_2 + 2k_3 + k_4) \end{aligned} \tag{24}$$

To compare the performance of the different numerical methods and projections of the LLG, we calculated a dynamical diagram of the system in H-J parameter space, using a 300×300 grid. For each pair of parameters, the LLG equation was integrated with the time step 0.5 ps, reconstructing a phase portrait of the system containing 50,000 points. The initial 40,000 points were discarded to consider the steady motion of the magnetization vector without any transitional effects. The Hausdorff dimension was calculated for resulting 10,000 points using the same algorithm. The obtained dynamical diagrams are illustrated in Fig. 6. Therefore, the difference in calculation times will be attributed only to the choice of the numerical method used to solve the equation and the particular representation of the LLG. The comparison of calculation times is given in the table.

As one can see from the table, the projection of the LLG equation has a pronounced influence on the calculation times, leading to a seven-time speed gain for the Cartesian and a

five-time speed gain for the stereographic projection in comparison with the LLG calculations in spherical coordinates. Within the same projection type, the variation of the calculation times is less impressive – the 1st order Euler method scores about 40-50%, and the 2nd order Heun method – 60-80% relative to the 4th order Runge-Kutta method.

Method / Projection	Euler	Heun	4th order Runge-Kutta
Cartesian	17^m58^s / (7%)	23^m57^s / (10%)	31^m43^s / (13%)
Spherical	$1^h40^m38^s$ / (42%)	$2^h28^m01^s$ / (61%)	$4^h1^m19^s$ / (100%)
Stereographic	20^m20^s / (8%)	26^m52^s / (11%)	46^m08^s / (19%)

Table 1. Calculation times for different integration methods and representations of LLG equation. The numbers in parenthesis give the (rounded) percentage, assigning 100% to spherical LLG calculated with 4th order Runge Kutta method (grey cell).

Let us analyze the dynamical diagrams presented in Fig. 6. At a first glance, the results obtained by the Euler method are drastically different from those obtained with higher-order methods. The IPP/OPP boundary is shifted to larger currents, but the difference does not consist in mere scaling – the data obtained by the Euler method features distinct oscillation modes (such as precession around the easy axis), which has no correspondence for the case of Runge-Kutta or Heun integration. One may argue that such low accuracy is caused by the fact that re-normalization of the magnetization vector **M** in the Cartesian system is not enough, since it does not take into account second order changes of the orientation of the magnetization vector. However, the very same situation takes place for the dynamical diagrams calculated with the Euler method using the spherical and stereographic projections, which reduce the number of degrees of freedom and automatically satisfy the condition of constant length of the magnetization vector **M**.

Curiously, the distortion of the dynamic diagrams slightly improves (so that the division line between IPP and OPP modes is shifted to lower currents) – perhaps, because the two-dimensional projection somewhat "lowers" the accumulated calculation error. In any case, the dynamic diagrams obtained with the Euler method are definitely wrong – for example, LLG written in the stereographic projection displays three IPP/OPP boundaries in the dynamic diagram, while the calculation made with a 2nd order method clearly show that there should be only *one* such boundary.

Therefore, comparison of accuracy and performance suggests that the Heun method is the most recommendable for fast and reliable solution of the LLG equation in different representations. To improve precision one should use the 4th order Runge-Kutta method, which, however, will mean at least doubled calculation times.

3.3 Stochastic case

The deterministic LLG equation, considered above, is applicable only for T=0K. At higher temperatures, the system is affected by thermal fluctuations due to the interaction of the magnetic moment with phonons, nuclear spins, etc. Due to this, the description of the magnetization dynamics becomes probabilistic, and can be found by solving the Fokker-Planck equation for the non-equilibrium distribution of the probability $P(M, t)$. This approach is very useful to magnetization reversal studies, allowing obtaining the probability

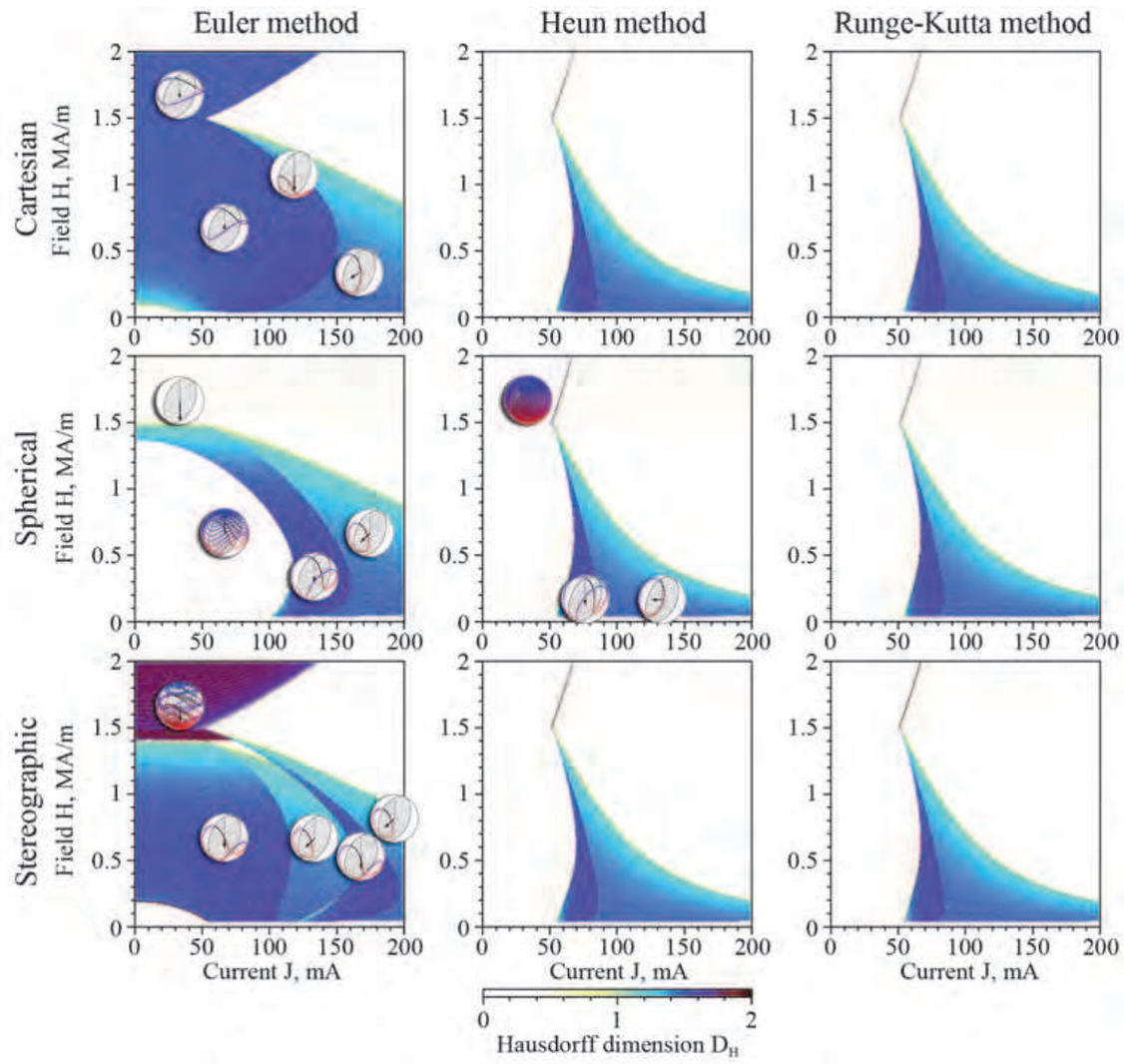

Fig. 6. Dynamic diagrams (based on the Hausdorff dimension D_H) calculated using 1st order Euler, 2nd order Heun and 4th order Runge-Kutta methods in Cartesian, spherical and stereographic projections. Integration step for all cases is 0.5 ps.

of switching under a given applied magnetic field, injected spin-polarized current *and* finite temperature, which is undoubtedly important for the development of magnetic memory devices. At the same time, for studies of magnetization precession it is desirable to have access to the time evolution of the magnetization vector, studying the phase portraits of the system as was done in the deterministic LLG case (García-Palacios & Lázaro 1998, Sukhov & Berakdar 2008). To do this, one should introduce the noise term to the effective field:

$$H_t = \sqrt{\frac{2\alpha kT}{\gamma_1 \mu_0 V M_S \Delta t}} W_t \,. \tag{25}$$

Here k is Boltzmann constant, T is temperature, V is the volume of magnetic particle and Δt is integration step for the time (referred above as h). The quantity W_t is the random variable

corresponding to a Wiener process with zero mean value and constant standard deviation. The noise term transforms the LLG into a stochastic differential equation (SDE)

$$\frac{1}{\gamma_1}\frac{d\mathbf{M}}{dt} = -\mathbf{M}\times(\mathbf{H}+\mathbf{H}_t+\alpha\mathbf{J}) + \frac{1}{M_S}\mathbf{M}\times(\mathbf{M}\times(\mathbf{J}-\alpha(\mathbf{H}+\mathbf{H}_t)) \tag{26}$$

As one can see, the current-induced torque does not contribute to the noise term, while the field-induced torque does. As vector products are distributive over addition, one can separate deterministic and noise parts of the equation

$$\frac{1}{\gamma_1}\frac{d\mathbf{M}}{dt} = \left[-\mathbf{M}\times\mathbf{\Lambda} + \frac{1}{M_S}\mathbf{M}\times(\mathbf{M}\times\mathbf{\Delta})\right] - \left[\mathbf{M}\times\mathbf{H}_t + \frac{1}{M_S}\mathbf{M}\times(\mathbf{M}\times\alpha\mathbf{H}_t)\right] \tag{27}$$

Here torque-inducing vectors $\mathbf{\Lambda}$ and $\mathbf{\Delta}$ are the same as those introduced for equation (3). The general form of such a SDE can be written as a sum of a drift (deterministic) and diffusion (noise) terms $f(y)$ and $g(y)$, respectively

$$dy = f(y)dt + g(y)dW_t\,. \tag{28}$$

This is a Langevin equation with multiplicative noise, because the noise term g depends on the phase variable $y \equiv \mathbf{M}$. To find the increment of the function during a finite time step dt the equation (28) should be integrated

$$dy = \int_t^{t+dt} f(y(t'),t')dt' + \int_t^{t+dt} g(y(t'),t')dW_{t'}dt'\,. \tag{29}$$

The deterministic integral is easy to find as the function $f(t)$ is a regular function. The situation with the stochastic term is radically different, because the function $g(y)$ includes a Wiener process that is non-differentiable. In the simplest case, one can estimate the value of the integral by evaluating $g(y)$ at the beginning of a small dt interval, assume it constant, and thus obtain the integral as multiplication $W_t dt^{1/2}$, because dW_t is proportional to the square root of the integration time step dt. Under these assumptions, one will obtain the Itô interpretation of the stochastic differential equation:

$$dy(t) = f(y(t),t)dt + g(y(t),t)W_t\sqrt{dt}\,. \tag{30}$$

The other option is to evaluate the diffusion term at an intermediate point belonging to the time interval $[t,\ t+dt]$ that would give rise to an additional drift term. If one chooses the intermediate point to be the midpoint of the aforementioned interval which, from the discussion of eq. (22) gives a second order algorithm, the stochastic equation can be rewritten as:

$$dy(t) = \left[f(y(t),t) + \tfrac{1}{2}g'(y(t),t)g(y(t),t)\right]dt + g(y(t),t)W_t\sqrt{dt}\,. \tag{31}$$

with the partial derivative $g'(y) = \partial g(y,t)/\partial y$. The latter formula corresponds to the Stratonovich interpretation of the SDE, where the usual chain rule of integration remains valid. As equations (30) and (31) are different, they will naturally lead to distinct solutions. One should then use the drift term appropriate to the interpretation being used (the Fokker-

Planck equation for the probability distribution is the same in both interpretations). The Itô interpretation is widely used for mathematical problems and for financial applications, in particular. It has the advantage that only requires information about past events. The Stratonovich interpretation is appropriate for physical and engineering systems (Kloeden & Platen, 1999), where Langevin equations are derived from microscopic models by a coarse-graining process. Therefore, to simulate magnetization dynamics governed by a stochastic LLG equation, one need to ensure that: 1) the appropriate method for the solution of the deterministic part of the LLG (i.e. at least a second-order numerical method) will be used; 2) this method will converge to the Stratonovich solution of the SDE; 3) the integration will be performed with a proper integration step so that $dt \sim dW^2$, requiring a smaller step for the case of higher temperatures; and 4) the random numbers used to generate the noise term of the stochastic equation will meet the requirements of a Wiener process.

The straightforward re-mapping of the Euler method to the stochastic case is known as the Euler-Maruyama method (Mahony, 2006):

$$y_{n+1} = y_n + \Delta_t f(y_n) + \Delta_{Wn} g(y_n) \,. \tag{32}$$

Similarly to the case of ODE, this method is easy to implement, but it gives unreliable results if the drift and diffusion terms vary significantly (which includes the case of magnetization dynamics simulations). The stochastic Euler method converges to the Itô solution (Kloeden & Platen 1999). To obtain the Stratonovich solution, one may introduce the additional drift term into the first-order numerical scheme, leading to the Milstein method (Mahony, 2006):

$$y_{n+1} = y_n + \Delta_t f(y_n) + \Delta_{Wn} g(y_n) + \tfrac{1}{2} g(y_n) g'(y_n)(\Delta_{Wn}^2 - \Delta_t) \tag{33}$$

This approach allows to increase the convergence order to unity, which is still insufficient for the LLG SDE. As we have shown before, the numerical method should be at least of the second order to allow proper treatment of the deterministic LLG. Therefore, the basic choice also points to the stochastic Heun method (Burrage, Burrage & Tian, 2004):

$$\widehat{y}_n = y_n + \Delta_t f(y_n) + \Delta_W g(y_n) \;\; y_{n+1} = y_n + \tfrac{1}{2}\Delta_t (f(y_n) + f(\widehat{y}_n)) + \tfrac{1}{2}\Delta_{Wn}(g(y_n) + g(\widehat{y}_n)) \tag{34}$$

It converges to the Stratonovich solution and is convenient for implementation as no additional drift term is necessary. Further precision improvement can be achieved by use of stochastic Runge-Kutta methods, such as second-order method (Mahony, 2006):

$$\widehat{y}_n = y_n + \tfrac{2}{3}\Delta_t f(y_n) + \tfrac{2}{3}\Delta_{Wn} g(y_n)$$

$$y_{n+1} = y_n + \Delta_t(\tfrac{1}{4} f(y_n) + \tfrac{3}{4} f(\widehat{y}_n)) + \Delta_{Wn}(\tfrac{1}{4} g(y_n) + \tfrac{3}{4} g(\widehat{y}_n)) \tag{35}$$

The Runge-Kutta methods also converge to the Stratonovich solution and do not require insertion of any additional drift terms.

The next important question is to ensure the proper characteristics of the noise. The basic generators of random numbers available in BASIC, FORTRAN, C or Pascal actually represent pseudo-random numbers, which repeat after a certain large number of steps. For the solution of stochastic differential equations, we should generate random numbers corresponding to a Wiener process, i.e., characterized by zero mean and constant dispersion.

One of the useful approaches is the Ziggurat method proposed by Marsaglia and Tsang (2000). It consists in binning of the area below the desired distribution curves with rectangles of the same area, the lowest of which tails to the infinity. Upon generation of an integer random number, its rightmost bits are counted as an index to the bin. If the random number fits below the distribution curve, it is used as an outcome of the algorithm; in the opposite case, the number becomes transformed until this condition is satisfied. By storing several arrays of coefficients describing the binning applied, it is possible to achieve fast generation of random numbers obeying the required decreasing distribution. Comparison of the Ziggurat method with other fast generators of random numbers show a considerable performance gain, requiring three-times less time than Ahrens-Dieter and 5.5 times – than Leva method (Marsaglia & Tsang, 2000).

For a three-dimensional system, one should use a 3D Wiener process for the thermal field. This means that we should create three independent sets of random numbers modifying the effective field components H_X, H_Y and H_Z. However, for practical application it is computation-costly to re-generate a whole set of random numbers if one is going to calculate the dynamic diagrams composed of dozens of thousands of points; additionally, as thermal fluctuations should be taken into account from a probabilistic point of view, it will be necessary to average over several different realizations of the stochastic process to obtain the required statistical data about the system. We suggest to improve this situation by pre-generating several sets of Wiener processes (which can be saved into a file for further use), and then to generate three non-repeating random numbers to pick independent stochastic "channels". This approach allows $P(n,k) = n!/(n - k)!$ permutations for channel number n grouped in $k = 3$ subsets. In our studies, n=20 pre-calculated channels were used, giving 6840 possible types of 3D Wiener processes. Increasing the number of pre-calculated channels to 50, one easily obtains over 10^5 possible combinations.

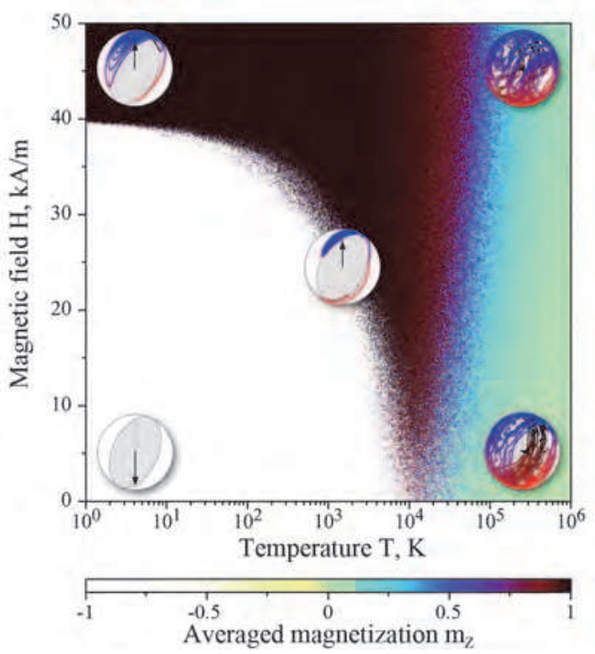

Fig. 7. The dynamic diagram of macrospin reversal with temperature. The plot is averaged over 20 realizations of Wiener process. The characteristic phase portraits are shown.

To illustrate the influence of the temperature on the macrospin dynamics, we present in Fig. 7 the dynamical diagram, averaged over 20 realizations of the stochastic process, for a macrospin in the parameter space (H, T). Here we focus on magnetization reversal, observing the change of normalized magnetization component $m_Z = M_Z / M_S$ allowing clear distinction between up / down magnetization states. As it is natural to expect, for the low temperatures (T < 10K) the border between $m_Z = \pm 1$ states is very sharp. The transition occurs upon application of magnetic field overcoming easy axis anisotropy, which is responsible for "holding" the magnetization in its stationary state. With increase of the temperature, the thermal fluctuations intensify and help the macrospin to overcome the potential barrier. At a certain temperature the fluctuations are so strong that the potential barrier created with the easy axis anisotropy is insufficient to separate the states with $m_Z = \pm 1$. Above this temperature the system becomes paramagnetic.

The overall qualitative behaviour of the system as illustrated in Fig. 7 is physically sound; however, a quantitative picture is far from perfect. One would expect the transition temperature to correspond to the Curie temperature, which for the model material (Co) is 1404K; the simulation plot shows that the loss of ferromagnetism occurs for temperatures about one order of magnitude higher. These unrealistic temperatures are a known problem with macrospin simulations (Xiao, Zangwill, & Stiles, 2005). They can be partially explained by the fixed length of the magnetization vector, while in real-life ferromagnetics the saturation magnetization decreases for increasing temperature. Therefore, the macrospin model is unrealistically "tough" to repolarise in the high-temperature mode, yielding an unrealistic Curie temperature. Indeed, if the magnetization vector is allowed to change its length – the approach used in the Landau-Lifshitz-Bloch equation – the simulation of the magnetization dynamics becomes more realistic at high temperatures (Chubykalo-Fesenko et al., 2006).

4. Conclusion

We analyzed different representations (spherical, Cartesian, stereographic and Frenet-Serret) of the Landau-Lifshitz-Gilbert equation describing magnetization dynamics. The fastest calculations are achieved for the equation written in Cartesian coordinates, which, however, requires re-normalization of the magnetization vector at every integration step. The use of spherical coordinates, despite being the straightforward approach for the system with constant **M**, is laden with trigonometric functions and requires larger calculation times.

The choice of the numerical method is also an important point for the simulations of magnetization dynamics. It was shown that the LLG *requires* at least a second-order numerical scheme to obtain the correct solution. Analysis of calculation performance suggests that the Heun method is a reasonable choice in terms of producing adequate results under acceptable calculation times.

For the case of finite-temperature modelling, the LLG becomes a stochastic equation with multiplicative noise, which makes it important to select the proper interpretation of the stochastic differential equation. Since this is a physical problem, it is usually more natural and favourable to consider the physical system in the framework of the Stratonovich interpretation, where the usual chain rule is still valid. The set of numerical methods suitable for its solution is then narrowed down. On the other hand, since it is possible to convert the SDE to the Itô interpretation, it is also possible to use the Itô integration as well, as we are dealing with the white thermal noise. Aiming to use minimally second-order

method for the deterministic LLG equation, we return to the suggestion that the Heun's scheme offers a reasonable accuracy. At the same time, the imposition of constant length of the magnetization vector (as it appears in the LLG) makes the system unrealistically stable at high temperatures, which results in a non-physical value of the Curie temperature. In order to achieve more realistic results, it is necessary to allow the variation of the magnetization vector length, which can be realized, for example, in the Landau-Lifshitz-Bloch equation.

5. Acknowledgment

The authors gratefully acknowledge the support by the grants of CONACYT as Basic Science Project # 129269 (México) and FCT Project PTDC/FIS/70843/2006 (Portugal).

6. References

Baibich, M.N.; Broto, J.M.; Fert, A.; Nguyen Van Dau, F.; Petroff, F.; Eitenne, P.; Creuzet, G.; Friederich A. & Chazelas J. (1988). Giant magnetoresistance of (001)Fe/(001)Cr magnetic superlattices, *Physical Review Letters*, Vol. 61, pp. 2472–2475, ISSN 0031-9007

Berkov, D.V. & Gorn, N.L. (2006). Micromagnetic simulations of the magnetization precession induced by a spin-polarized current in a point-contact geometry, *Journal of Applied Physics*, Vol. 99, 08Q701, ISSN 0021-8979

Burrage, K.; Burrage P.M., & Tian, T. (2004). Numerical methods for strong solutions of SDES, *Proceedings of the Royal Society, London*, Vol. 460, pp. 373–402, ISSN 0950–1207

Chubykalo-Fesenko, O.; Nowak, U.; Chantrell, R.W. & Garanin, D. (2006). Dynamic approach for micromagnetics close to the Curie temperature, *Physical Review B*, Vol. 74, 094436, ISSN 1098-0121

Donahue, M.J. & McMichael, R.D. (2007). Micromagnetics on curved geometries using rectangular cells: error correction and analysis, *IEEE Transactions on Magnetics,* Vol. 43, pp. 2878-2880, ISSN 0018-9464

Fidler, J. & Schrefl, T. (2000). Micromagnetic modelling—the current state of the art. *Journal of Physics D: Applied Physics*, Vol. 33, pp. R135–R156, ISSN 0022-3727

García-Cervera, C.J.; Gimbutas, Z. & Weinan, E. (2003). Accurate numerical methods for micromagnetics simulations with general geometries, *Journal of Computational Physics*, Vol. 184, pp. 37–52, ISSN 0021-9991

García-Palacios, J.L. & Lázaro, F.J. (1998). Langevin-dynamics study of the dynamical properties of small magnetic particles, *Physical Review B*, Vol. 58, pp. 14937–14958, ISSN 1098-0121

Gilbert T.L. (2004). A phenomenological theory of damping in ferromagnetic materials, *IEEE Transactions on Magnetics,* Vol. 40, pp. 3443-3449, ISSN 0018-9464

Horley, P.P.; Vieira, V.R.; Gorley, P.M.; Dugaev, V.K.; Berakdar, J. & Barnaś, J. (2008). Influence of a periodic magnetic field and spin-polarized current on the magnetic dynamics of a monodomain ferromagnet, *Physical Review B*, Vol. 78, pp. 054417, ISSN 1098-0121

Horley, P.P.; Vieira, V.R.; Sacramento, P.D. & Dugaev, V.K. (2009). Application of the stereographic projection to studies of magnetization dynamics described by the Landau–Lifshitz–Gilbert equation, *Journal of Physics A: Mathematical and Theoretical*, Vol. 42, 315211, ISSN 1751-8113

Kiselev, S.I.; Sankey, J.C.; Krivorotov, I.N.; Emley, N.C.; Schoelkopf, R.J.; Buhrman, R.A. & Ralph, D.C. (2003). Microwave oscillations of a nanomagnet driven by a spin-polarized current, *Nature*, Vol. 425, pp. 380–383, ISSN 0028-0836

Kloeden, P.E. & Platen, E. (1999). *Numerical solution of stochastic differential equations*, Springer Verlag, ISBN 3-540-54062-8, Berlin

Koehler, T.R. & Fredkin D.R. (1992). Finite element method for micromagnetics, *IEEE Transactions on Magnetics,* Vol. 28, pp. 1239-1244, ISSN 0018-9464

Lichtenberg, A.J. & Lieberman, M.A. (1983). *Regular and stochastic motion*. Springer-Verlag, ISBN 3-540-90707-6, Berlin-Heidelberg-New York

Liu, Z.J.; Long, H.H.; Ong, E.T., & Li, E.P. (2006). A fast Fourier transform on multipole algorithm for micromagnetic modeling of perpendicular recording media, *Journal of Applied Physics*, Vol. 99, 08B903, ISSN 0021-8979

Mahony, C.O. (2006). The numerical analysis of stochastic differential equations, Available from http://citeseerx.ist.psu.edu/viewdoc/summary?doi=10.1.1.117.8043

Marsaglia, G. & Tsang, W.W. (2000). The Ziggurat method for generating random variables, *Journal of Statistical Software*, Vol. 5, pp. 1–7, ISSN 1548-7660

Mills, D.L. & Arias, R. (2006). The damping of spin motions in ultrathin films: Is the Landau–Lifschitz–Gilbert phenomenology applicable? *Physica B*, Vol. 384, pp. 147–151, ISSN 0921-4526

Normand, J.M. & Raynal, J. (1982). Relations between Cartesian and spherical components of irreducible Cartesian tensors, *Journal of Physics A: Mathematical and General*, Vol. 15, pp. 1437–1461, ISSN 0305-4470

Parker, G.J.; Cerjan, C., & Hewett, D.W. (2000). Embedded curve boundary method for micromagnetic simulations, *Journal of Magnetism and Magnetic Materials*, Vol. 214, pp. 130-138, ISSN 0304-8853

Saradzhev, F.M.; Khanna, F.C.; Sang Pyo Kim & de Montigny, M. (2007). General form of magnetization damping: Magnetization dynamics of a spin system evolving nonadiabatically and out of equilibrium, *Physical Review B*, Vol. 75, 024406, ISSN 1098-0121

Schabes, M.E. & Aharoni, A. (1987). Magnetostatic interaction fields for a three-dimensional array of ferromagnetic cubes, *IEEE Transactions on Magnetics,* Vol. MAG-23, pp. 3882-3888, ISSN 0018-9464

Scholz, W.; Fidler, J.; Schrefl, T.; Suess, D.; Dittrich, R.; Forster, F. & Tsiantos, V. (2003). Scalable parallel micromagnetic solvers for magnetic nanostructures, *Computational Materials Science*, Vol. 28, pp. 366–383, ISSN 0927-0256

Slonczewski, J.C. (1996). Current-driven excitation of magnetic multilayers, *Journal of Magnetism and Magnetic Materials*, Vol. 159, pp. L1-L7, ISSN 0304-8853

Sukhov, A. & Berakdar, J. (2008). Temperature-dependent magnetization dynamics of magnetic nanoparticles, *Journal of Physics: Condensed Matter*, Vol. 20, 125226, ISSN 0953-8984

Szambolics, H.; Buda-Prejbeanu, L.D.; Toussaint, J.C. & Fruchart, O. (2008). A constrained finite element formulation for the Landau–Lifshitz–Gilbert equations, *Computational Materials Science*, Vol. 44, pp. 253–258, ISSN 0927- 0256

Tan, X.; Baras, J.S. & Krishnaprasad P.S. (2000). Fast evaluation of demagnetizing field in three dimensional micromagnetics using multipole approximation, *Proceedings SPIE*, Vol. 3984, pp. 195-201, ISSN 0277-786X

Tiberkevich, V. & Slavin, A. (2007). Nonlinear phenomenological model of magnetic dissipation for large precession angles: Generalization of the Gilbert model, *Physical Review B*, Vol. 75, 014440, ISSN 1098-0121

Vukadinovic, N. & Boust, F. (2007). Three-dimensional micromagnetic simulations of magnetic excitations in cylindrical nanodots with perpendicular anisotropy, *Physical Review B*, Vol. 75, 014420, ISSN 1098-0121

Xiao, J.; Zangwill, A. & Stiles, M.D. (2005). Macrospin models of spin transfer dynamics, *Physical Review B*, Vol. 72, 014446, ISSN 1098-0121

Žutic, I.; Fabian J. & Das, S. (2004). Spintronics: fundamentals and applications, *Reviews of Modern Physics*, Vol. 76, pp. 323–410, ISSN 0034-6861

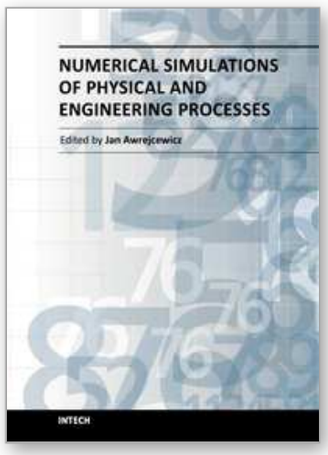

Numerical Simulations of Physical and Engineering Processes

Edited by Prof. Jan Awrejcewicz

ISBN 978-953-307-620-1
Hard cover, 594 pages
Publisher InTech
Published online 26, September, 2011
Published in print edition September, 2011

Numerical Simulations of Physical and Engineering Process is an edited book divided into two parts. Part I devoted to Physical Processes contains 14 chapters, whereas Part II titled Engineering Processes has 13 contributions. The book handles the recent research devoted to numerical simulations of physical and engineering systems. It can be treated as a bridge linking various numerical approaches of two closely inter-related branches of science, i.e. physics and engineering. Since the numerical simulations play a key role in both theoretical and application oriented research, professional reference books are highly needed by pure research scientists, applied mathematicians, engineers as well post-graduate students. In other words, it is expected that the book will serve as an effective tool in training the mentioned groups of researchers and beyond.

How to reference

In order to correctly reference this scholarly work, feel free to copy and paste the following:

Paul Horley, Vítor Vieira, Jesús González-Hernández, Vitalii Dugaev and Jozef Barnas (2011). Numerical Simulations of Nano-Scale Magnetization Dynamics, Numerical Simulations of Physical and Engineering Processes, Prof. Jan Awrejcewicz (Ed.), ISBN: 978-953-307-620-1, InTech, Available from: http://www.intechopen.com/books/numerical-simulations-of-physical-and-engineering-processes/numerical-simulations-of-nano-scale-magnetization-dynamics

INTECH
open science | open minds

InTech Europe
University Campus STeP Ri
Slavka Krautzeka 83/A
51000 Rijeka, Croatia
Phone: +385 (51) 770 447
Fax: +385 (51) 686 166
www.intechopen.com

InTech China
Unit 405, Office Block, Hotel Equatorial Shanghai
No.65, Yan An Road (West), Shanghai, 200040, China
中国上海市延安西路65号上海国际贵都大饭店办公楼405单元
Phone: +86-21-62489820
Fax: +86-21-62489821

IntechOpen